Design and Modeling of a Parallel-Pipe-Crawling Pneumatic Soft Robot

ZHIYUAN ZHANG [ID] **[1], XUEQIAN WANG** [ID] **[1], SONGTAO WANG[2],**
DESHAN MENG[1], AND BIN LIANG[1,2,3], (Member, IEEE)
[1]Center for Artificial Intelligence and Robotics, Tsinghua Shenzhen International Graduate School, Shenzhen 518055, China
[2]Research Institute of Tsinghua University at Shenzhen, Shenzhen 518057, China
[3]Navigation and Control Research Center, Department of Automation, Tsinghua University, Beijing 100084, China

Corresponding authors: Xueqian Wang (wang.xq@sz.tsinghua.edu.cn) and Bin Liang (liangbin@tsinghua.edu.cn)

ABSTRACT Soft robots have unique advantages over traditional rigid robots and have broad application prospects in many fields, such as pipe inspections. Several of the reported pipe-crawling soft robots have long actuation periods and small locomotion speeds. Moreover, they lack active steering property to adapt to complex piping systems, such as T-shaped pipes. To solve the above problems, this paper proposes a novel parallel-pipe-crawling pneumatic soft robot consisting of three extensible pneumatic soft actuators and two flexible feet. The parallel structure and flexible feet allow the robot to reduce the number of steps in a crawling cycle. The extensible actuator allows the robot to change its body shape for active steering property. However, a complete mathematical model for soft robots with parallel structure is hard to establish. In this paper, the phenomenological modeling method is used to realize a mathematical model with high precision, limited calculation, and easy engineering applicability of the pipe-crawling soft robot. Then, the prototype of the robot is fabricated with the optimal structural parameters selected by finite element simulations. The static identification experiment shows that the average errors of the extended length and output force are 0.51 mm and 0.28 N, respectively. The crawling experiments in various scenarios show that the horizontal crawling speed is higher than 15 mm/s, the maximum load is 2.456 kg, and the minimum turning radius is 38.2 mm. The robot shows great potential for inspecting in complex pipes with high crawling efficiency, excellent flexibility, and strong adaptability by switching its crawling gaits.

INDEX TERMS Finite element simulation, parallel, phenomenological modeling, pipe-crawling robot, soft robot.

I. INTRODUCTION

Pipes provide low-cost transportation for materials such as oil, natural gas, and sewage. To handle high pressure and avoid flammable explosion of the transported objects, the pipes must fulfill high demands of safety, reliability, and efficiency [1]. However, pipes are easily deformed and cracked because of long-term use, chemical corrosion, and material aging. Leakage from the pipe will cause problems such as supply fluctuations, wastage of resources, and environmental pollution, and even lead to serious consequences such as explosions that endanger personal safety. Therefore, pipes need to be inspected, cleaned, and maintained

frequently [2]. Owing to the complexity and number of pipe networks, workers cannot directly inspect pipes in narrow spaces. Therefore, pipe robots are required to perform pipe inspections and maintenance tasks.

The pipe robot is a special robot that can carry sensors and tools and automatically move outside [3] or inside the pipe to complete different operations [4]. Researchers have developed differential pressure robots [5], [6], wheeled robots [7]–[9], legged robots [10], [11], spiral robots [12], [13], peristaltic robots [14], snake-like robots [15]–[17], and the like to navigate inside pipes or narrow spaces. However, each of these robots had problems. For example, the pipeline pig used fluid to move forward passively, which caused the traction to be unregulated. Although the wheeled robot had a stable motion speed and large traction, they were

---

The associate editor coordinating the review of this manuscript and approving it for publication was Luigi Biagiotti.

bulky and only suitable for pipes having large diameters and hard materials to avoid secondary damage. The legged robot moved at a fast speed and was easy to operate, but the motion speed was unstable. Moreover, although the snake-like robot was more flexible, it was difficult for the robot to crawl in a vertical pipe.

Pipe-crawling soft robots have been widely studied to solve the problems faced by rigid robots and further improve the safety, flexibility, and intelligence of robots [18]. However, in previous studies of pipe-crawling soft robots, the robot was always designed on a modular scheme, based on which they could be divided into peristaltic robots and spiral robots. Most peristaltic soft robots have a series structure. The motion cycle is mostly earthworm-like. In the first step, the rear contracted actuator is anchored to the pipe; in the second step, the extensible actuator is elongated to reach a farther point; in the third step, the frontal contracted actuator is anchored to the pipe; in the fourth step, the rear contracted and extensible actuators are relaxed; in the fifth step, the rear and frontal contracted actuators are anchored to the pipe. For example, the robot designed by Connolly *et al.* [19] consisted of four pneumatic actuation modules in series, namely, two contracted modules, one extended module, and one torsion module. Calderón *et al.* [20] designed a robot consisting of a contracted actuator, an extensible actuator, and a contracted actuator in sequence. Yamazaki *et al.* [21] designed a robot that consisted of 25 actuators. These robots could crawl and passively turn by mimicking the earthworm-like gait. Gilbertson *et al.* [22] also designed a robot with three actuators. The difference between this robot and that proposed in [20] is that the first and third segments were replaced by spiral actuators to anchor to the pipe wall. The motion cycle was unchanged. With regard to spiral soft robots, the robot designed by Takeshima and Takayama [23], [24] had a new structure consisting of six braided tubes, which included a right-hand helix [25] and a left-hand helix. The robot could rotate in both directions in pipes of various diameters based on the pressurization patterns of the six actuators.

The above pipe-crawling soft robots have the following common characteristics: (1) many peristaltic robots are connected in series by different types of actuators. They mimic the crawling motion of the earthworm. However, the crawling period is long and the locomotion speed is small. Nevertheless, the movement of the spiral robot is more complicated. (2) These robots do not have active steering property. They can only crawl through a single pipe and cannot adapt to complex piping systems, such as Y-shaped and T-shaped pipes, where they will be required to actively select the steering direction. (3) Detection devices cannot be installed on the robotic body, and the actual condition of the opaque pipe cannot be fed back because of which the pipe inspection task cannot be completed satisfactorily.

In summary, it is necessary to design a novel pipe-crawling soft robot with improved crawling efficiency, which can steer actively and adapt itself to many types of pipes. Research on such a robot will have important theoretical research significance and engineering application value.

Based on the concept of modular design, this paper proposes a novel parallel pipe-crawling pneumatic soft robot, which consists of three extensible pneumatic soft actuators (ePSA), three connecting rings, and two flexible feet. The structural innovations of the proposed design are as follows:

(1) The parallel structure allows the robot to reduce the number of steps in a crawling cycle. The robot only needs two steps of inflation and deflation to generate one stride, which can improve the crawling efficiency.

(2) The flexible feet give the robot an excellent crawling property. When the contact surface and contact area between the feet and the pipe wall is changed, the direction of friction changes. Thus the robot can move forward or backward.

(3) The ePSA allows the robot to change its body shape to have active steering property. The different pressurization patterns of the three ePSAs allow the robot to achieve three degrees of freedom in pitch, yaw, and extension motion in 3D space.

(4) There is room at the center line of the robot to carry devices such as endoscopic cameras to feed back the actual condition inside the opaque pipeline. After designing the robot, we use finite element simulations to analyze several key parameters that may affect the performance of the robot, such as the radius of the air chamber, the number of fiber winding turns, the groove height of the feet, and the number of connecting rings. Then, the optimal structural parameters of the robot are selected.

Although the parallel structure of three or four pneumatic soft actuators has been recently presented [26]–[28], no researchers applied this structure to soft crawling robots, and the mathematical modeling problem of parallel structures has not been well solved.

The mathematical modeling of the parallel-pipe-crawling soft robot is divided into two parts: (1) the dynamics/statics model of the ePSA; (2) the kinematics model and inverse kinematics model of the robot. The model of the ePSA is complex owing to the nonlinear response of soft materials such as silicone elastomers. Presently, many researchers use experimental fitting methods to describe the relationship between the levels of the input air pressure and the length of the ePSA [29], [30]. Trivedi *et al.* [31] established the dynamic model of the pneumatic manipulator based on the Cosserat rod theory. Zheng *et al.* [32] used distributed elastic and damping forces to express the diastolic state of the muscle. Tatlicioglu *et al.* [33] established a dynamic model of the 2D soft robot by considering the gravitational potential energy and elastic potential energy stored in it. Qi *et al.* [34] modeled the equilibrium relationship between the driving torque generated by the input air pressure and the counter torque generated by the silicone rubber. Laschi *et al.* [35] modeled their robot based on the principle of virtual work and the assumption of constant curvature. These previous studies on soft robot have the following disadvantages: (1) most of the

applications of these models have no axial degree of freedom. (2) Although a small number of applications have extensible freedom, few researchers have applied it to the case where the robotic base can move. (3) The calculations of these models are huge and require multiple integral operations, making them difficult to respond quickly in engineering applications. In this paper, we wish to establish a mathematical model that has high precision, limited calculation, and easy engineering applicability for the parallel-pipe-crawling soft robot.

We utilize the phenomenological model proposed by Reynolds *et al.* to describe the property of our ePSA [36]. The phenomenological model is relatively simple and is commonly used to describe artificial pneumatic muscles, which mimic biological muscles by contracting and extending when pressure changes in the air chamber. The ePSA can be analogized to the previous artificial pneumatic muscle [36]. Based on reverse thinking, we replace the contraction force in the model with the thrust, so that the ePSA is equivalent to a three-element model consisting of a thrust element, a spring element, and a damping element in parallel.

With regard to the kinematics model, the robot is considered as one constant curvature arc in mainstream approaches and the kinematics model is studied under the constant curvature condition. A comprehensive review of this is presented in [37], [38]. In their work, a unified constant-curvature kinematics model considered three spaces, namely, actuator, configuration, and task, connected by two mappings, robot-independent and robot-specific. Based on this work, we establish the kinematics model and inverse kinematics model of our pipe-crawling soft robot. The 3D space shape of the robot is described by the curvature, bending angle, and torsion angle. Then, the homogeneous matrix of the configuration space transformation to the workspace is described by the Denavit–Hartenberg (D–H) transformation method. Based on this, we calculate the change in the position of the robotic rear foot after deflation. In addition, the trajectory planning method of the soft crawling robot in the pipe is proposed.

Thus, the mathematical model and trajectory planning method of the crawling soft robot is completely established, which can lay the foundation for high-precision servo closed-loop control of the robot.

The rest of the paper is organized as follows. In Section II, the structural design of the pipe-crawling soft robot is described. In Section III, the statics model of the ePSA and the kinematics model and inverse kinematics model of the robot are established. In Section IV, the process for updating the position of the rear foot after each crawling cycle is demonstrated and the trajectory planning method is described. In Section V, the finite element simulations of the ePSA, the flexible foot, and the robot are performed to select the optimal parameters. We then demonstrate the workspace of motion at different air pressure levels. In Section VI, a prototype of the crawling robot is fabricated using 3D printing molds. In Section VII, the crawling locomotion of the robot is verified in several scenarios, such as a horizontal pipe, a vertical pipe, an L-shaped pipe, a bellows, an opaque

pipe, and a textured surface. In Section VIII, conclusions are drawn.

II. DESIGN

A. SINGLE EXTENSIBLE PNEUMATIC SOFT ACTUATOR

The ePSA uses the inflated air pressure to achieve axial elongated motion. As shown in Fig. 1, the ePSA consists of an elastic body, fiber winding wires, and a sealed head. Its elongated cylindrical body is fabricated with a hyperelastic silicone and has an inflatable air chamber on the inner center-line. When the air chamber is inflated, the ePSA will not only extend in the axial direction, but also expand radially [39]. To improve the actuating effect and avoid unnecessary expansion, the fiber wires are wound in a double helix on the surface of the ePSA. The number of turns of the fiber winding wire is one of the important factors affecting the performance of the ePSA. If the number of turns is too large, the ePSA will require higher input air pressure. On the contrary, if the number of turns is too small, the radial expansion will be higher. The appropriate number of turns will be selected by finite element simulation. In addition, the seal head is used to prevent air leakage.
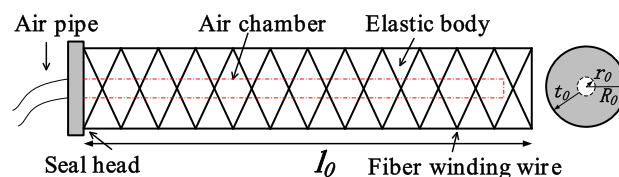
FIGURE 1. Design of extensible pneumatic soft actuator. l_0, R_0, r_0, and t_0 are the ePSA length, ePSA radius, air chamber radius, and wall thickness, respectively, in the initial state.

The ePSA has a simple structure and low fabricating requirements, which is convenient for developing a finite element model and a prototype. Moreover, it can be used to easily form a flexible and adaptable soft structure. When multiple ePSAs are combined in parallel, they can extend together at the same level of air pressure for increased stiffness. When different ePSAs have different inflated pressures, they can generate other bending motions with different bending and torsion angles [40].

B. PIPE-CRAWLING SOFT ROBOT

Although a single ePSA can only extend in the axial direction, three ePSAs can be combined into one soft robot with three degrees of freedom of pitch, yaw, and extension. The pipe-crawling soft robot consists of three ePSAs, several connecting rings, a frontal foot, and a rear foot, as shown in Fig. 2. The robot can also carry endoscope cameras, wireless cameras, and other devices necessary for pipe inspections.

The three ePSAs are uniformly distributed on the circumference and are connected by several intermediate inextensible connecting rings. They are independently controlled. When the three actuators are inflated at the same level of air pressure, $P_1 = P_2 = P_3$, the robot will extend along the axis. When the three actuators are inflated with different
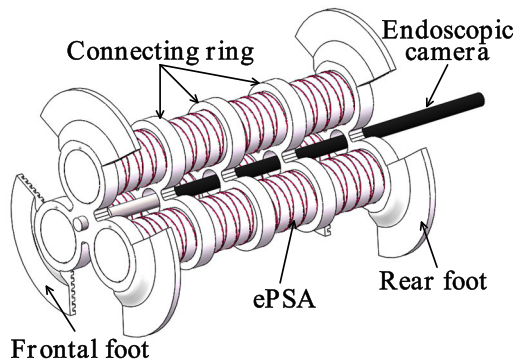
FIGURE 2. Design of pipe crawling soft robot.

air pressures, the robot will bend to the side having the smaller air pressure. In addition, when the size of the connecting rings is constant, the number of connecting rings is an important factor affecting the performance of the robot. If the number of connecting rings is too small, the successful combination of the three ePSAs into a flexible and adaptable soft robot cannot be achieved. On the contrary, if the number is too large, the coupling between the three ePSAs will be tight, making it challenging to establish a mathematical model and fabricate a physical prototype. The appropriate number of connecting rings will be selected by finite element simulation.

According to basic physics, the sliding friction between the rigid bodies is related to the positive pressure and the friction coefficient. It is well known that the coefficient of friction is only related to the condition between the contact faces, and is independent of the vertical pressure, the apparent contact area, and the sliding rate. However, the friction between the rubber and the rigid body is different. Due to the elastic deformation of the contact surface, the friction phenomenon is much more complicated, and the friction coefficient is no longer a fixed value. It is significantly affected by the vertical pressure, the sliding rate, and the temperature [41]. For rubber friction, it usually consists of three kinds of friction: adhesive friction, hysteresis friction (deformation loss friction), and air pocket friction (including other friction caused by special conditions) [42].

According to reference [43], the design of the flexible foot is shown in Fig. 3. The robot can crawl in the pipe with its two feet. The front surface of the foot is smooth and the back surface is engraved with grooves. The friction between the smooth surface of the foot and the pipe wall is small, allowing the robot to move forward. Since the roughness of the contact surface is increased, the groove surface has larger adhesive friction and hysteresis friction, which provides anchoring force to the robot. By changing the contact surface and contact area of the feet with the pipe wall, the robot can realize forward, backward, and steering locomotion in the pipe. In addition, when the number of grooves is constant, the groove height is an important factor affecting the performance of the robot. If the height is too large, the foot cannot withstand the large strain. On the contrary, if the

height is too small, the foot cannot change direction flexibly. The appropriate groove height will also be selected by finite element simulation.
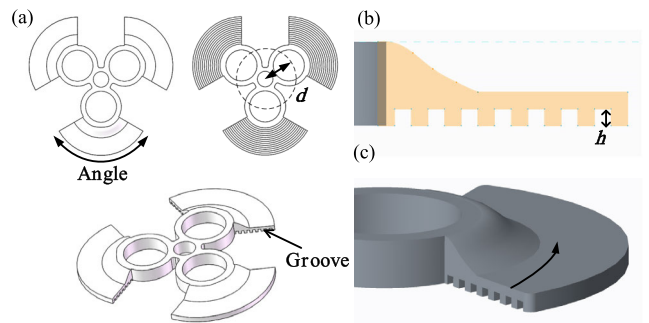

FIGURE 3. Design of flexible foot. (a) Design block diagram. (b) Scanning section. (c) Scanning direction. The front surface of the foot is smooth and the back surface is engraved with grooves. The angle is used to describe the contact area, *d* is the distance from the foot center to the sub circle center, *h* is the groove height.

As shown in Fig. 4, a crawling cycle includes two steps. First, when the ePSAs are inflated, the rear foot is flipped by the extension force. And the contact area between the groove surface of the rear foot and the pipe wall is passively increased to increase the friction. Consequently, the rear foot is anchored to the pipe. Then, the frontal foot is extended forward because the friction is smaller than the extension force. Next, when the ePSAs are deflated, the friction between the rear foot and the pipe wall and the frontal foot will be flipped to increase the friction between the frontal foot and the pipe wall. Consequently, the position of the frontal foot remains unchanged, whereas the rear foot is contracted forward. In addition, when the diameter of the pipe is small, the robot cannot cause enough friction to flip the contact surface of the flexible foot directly, but the crawling action can still be achieved based on the tendency of the flipping. Because the friction generated by a flexible foot with a tendency to flip is greater than that generated by a flexible foot that does not tend to flip. Therefore, when the diameter of the pipe is small, by changing the initial contact surfaces of each foot, the tendency of each foot will be changed during inflating, so the forward locomotion can be changed to backward locomotion.
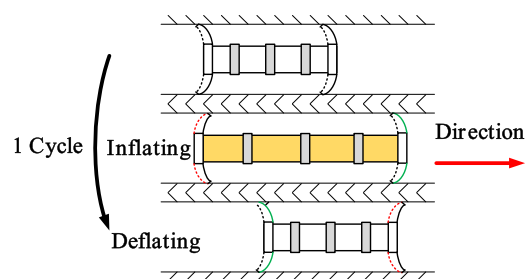

FIGURE 4. Two steps used by the robot to crawl one stride. In the first step, the ePSAs are inflated. In the second step, the ePSAs are deflated. The flexible feet move passively.

III. MATHEMATICAL MODELING

A. OPERATING SPACE

The operating space of the robot is shown in Fig. 5. The mathematical modeling process is divided into two parts: (1) statics modeling of a single ePSA, where the ePSA lengths $\{l_1, l_2, l_3\}$ are calculated based on the input air pressures $\{P_1, P_2, P_3\}$; (2) kinematics modeling of the robot, where the configuration space parameter, curvature, bending angle, and torsion angle $\{k, \theta, \phi\}$ of the robot are calculated using the ePSA lengths $\{l_1, l_2, l_3\}$. Then, the position $\{x, y, z\}$ of the end of the robot in Cartesian space is calculated based on the configuration space parameter. The challenging tasks are establishing the statics model of the ePSA, the coupling of each ePSA, and the inverse kinematics of the robot.
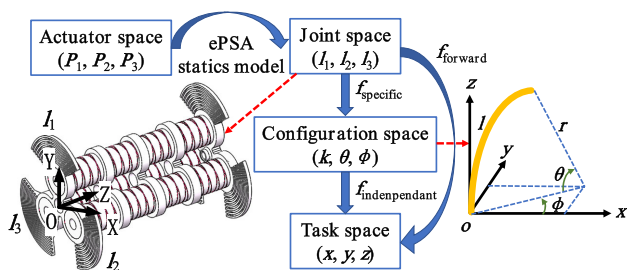
FIGURE 5. Overview of modeling process of the robot. Four spaces actuator, joint, configuration, and task with the connections by three mappings, ePSA statics model, robot-independent and robot-specific. According to the coordinate system of the robotic base, the robot can be abstracted into a constant curvature curve in 3D space.

B. STATICS MODELING OF SINGLE ePSA

The Voight equivalent model [44], [45] of the ePSA is established according to the structure and property of the ePSA described in Section II-A and the phenomenological modeling theory. Based on reverse thinking, we replace the contracted force in the Voight model with the thrust so that the ePSA is equivalent to a three-element model comprising a thrust element, spring element, and damping element in parallel, as shown in Fig. 6.
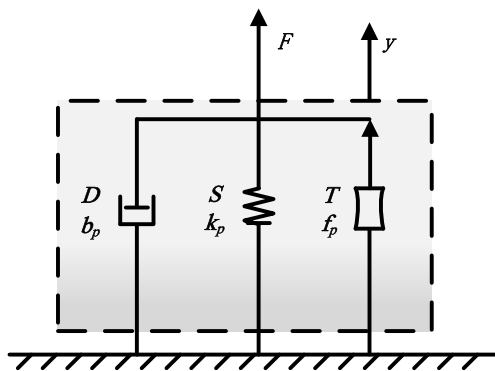
FIGURE 6. Equivalent model of the ePSA. A three-element model comprising a thrust element, spring element, and damping element in parallel.

In the dynamic model, the damping parameter is closely related to the dynamic characteristics of the ePSA, which directly affects the speed of extension. The spring parameter and the extended length of the ePSA are strongly related. However, the thrust parameter does not directly affect other variables; it is determined by the characteristics of the ePSA itself. According to [36], these three parameters are linearly related to the input air pressure. Then, the dynamic model of the ePSA can be expressed as

$$m\ddot{y} + b_p\dot{y} + k_p y + mg = f_p, \quad (1)$$

where m is the mass, g is the acceleration of gravity, and y, $\dot{y}$, and $\ddot{y}$ are the displacement, velocity, and acceleration of the ePSA, respectively. The nonlinear parameters b_p, k_p, and f_p are the parameters of damping, spring, and thrust, respectively. These parameters are given as

$$\begin{cases} f_p = f_1 P + f_0, \\ k_p = k_1 P + k_0, \\ b_p = b_1 P + b_0. \end{cases} \quad (2)$$

When ignoring the dynamic process, the acceleration and velocity are both 0, and the statics model of the ePSA can be obtained as

$$k_p y + mg = f_p, \quad (3)$$

where the relationship between the spring parameter k_p, the thrust parameter f_p, and the input air pressure can be obtained by static identification experiments.

C. KINEMATICS MODELING OF THE SOFT ROBOT

According to a study on constant curvature, the kinematics and inverse kinematics model of the robot should be based on the following assumptions [29]:

(a) The input air pressure acts uniformly on the inner surface of the air chamber; the air chamber radius of a single ePSA is constant at different cross sections; and the air chambers of the three ePSAs are parallel.

(b) The curved shape of the robot conforms to the constant curvature configuration, namely, when the robot is abstracted into a curve, the curvature of each part is constant.

(c) The robot always has one end fixed in each crawling cycle. For example, during the forward locomotion, the rear foot is fixed during the inflation process whereas the frontal foot is fixed during the deflation process.

(d) To reduce the complexity of modeling, the robot is analyzed without gravity and load.

According to the statics model of the ePSA, the ePSA lengths $\{l_1, l_2, l_3\}$ of the three ePSAs can be calculated. Then, based on the coordinate system shown in Fig. 5 and the method for solving the forward transformation questions described in [37], the configuration space parameters $\{k, \theta, \phi\}$ of the robot can be easily obtained as

$$k = \frac{1}{r} = \frac{2\sqrt{l_1^2 + l_2^2 + l_3^2 - l_1 l_2 - l_1 l_3 - l_2 l_3}}{d(l_1 + l_2 + l_3)}, \quad (4)$$

$$\theta = \frac{2\sqrt{l_1^2 + l_2^2 + l_3^2 - l_1 l_2 - l_1 l_3 - l_2 l_3}}{3d}, \tag{5}$$

$$\phi = \tan^{-1}(\frac{l_2 + l_3 - 2l_1}{\sqrt{3}(l_2 - l_3)}), \tag{6}$$

where l_i ($i = 1,2,3$) denotes the length of the three ePSAs, and d is the distance between the robot centerline and the ePSA centerline (i.e., the distance d of the flexible foot). Because of the coupling effect of the three ePSAs, d should be described in terms of the input air pressures $\{P_1, P_2, P_3\}$ and the physical distance d_0 as

$$d = d_0 + f(P_1, P_2, P_3). \tag{7}$$

Then, the position $\{x, y, z\}$ of the end of the robot in Cartesian space is calculated based on the configuration space parameter. According to the above assumptions, when the robot is abstracted into a curve, the relationship between the base coordinate system and the end coordinate system of the robot can be described by the homogeneous transformation matrix as

$$T = \begin{bmatrix} R & P_d \\ 0 & 1 \end{bmatrix}, \tag{8}$$

where R is the rotation matrix and P_d is the translation vector. It can be seen from Fig. 5 that the transformation process includes four steps: (1) the coordinate system is rotated by the torsion angle ϕ around the z-axis; (2) the coordinate system is rotated by the bending angle θ around the y-axis; (3) the coordinate origin is translated by P_d; (4) and the coordinate system is rotated by the torsion angle $-\phi$ around the z-axis. Therefore, the final form of the transformation matrix is

$$
\begin{aligned}
T &= \begin{bmatrix} R_z(\phi) & 0 \\ 0 & 1 \end{bmatrix} \begin{bmatrix} R_y(\theta) & P_d \\ 0 & 1 \end{bmatrix} \begin{bmatrix} R_z(-\phi) & 0 \\ 0 & 1 \end{bmatrix} \\
&= \begin{bmatrix} c^2\phi c\theta + s^2\phi & c\phi s\phi(c\theta - 1) & c\phi s\theta & c\phi(1 - c\theta)/k \\ c\phi s\phi(c\theta - 1) & s^2\phi c\theta + c^2\phi & s\phi s\theta & s\phi(1 - c\theta)/k \\ -c\phi s\theta & -s\phi s\theta & c\theta & s\theta/k \\ 0 & 0 & 0 & 1 \end{bmatrix},
\end{aligned} \tag{9}
$$

where $c\theta = \cos\theta$, $s\theta = \sin\theta$, $c\phi = \cos\phi$, and $s\phi = \sin\phi$.

D. INVERSE KINEMATICS MODELING OF THE SOFT ROBOT

The inverse kinematics model involves the calculation of the configuration space parameters $\{k, \theta, \phi\}$ and the ePSA lengths $\{l_1, l_2, l_3\}$ of the robot based on the Cartesian space position $\{x, y, z\}$ of the end. The inverse kinematics has great significance for soft robots. It improves the ability of real-time control, trajectory planning, obstacle avoidance, and the fault tolerance [29]. From (9), the parameters $\{k, \theta, \phi\}$ can be calculated from the position $\{x, y, z\}$ as

$$\phi = \tan^{-1}(\frac{y}{x}), \tag{10}$$

$$\theta = \tan^{-1}(\frac{z}{\sqrt{x^2 + y^2}}), \tag{11}$$

$$k = \frac{\sin\theta}{z}. \tag{12}$$

Reference [46] proposes methods to solve such inverse transformations. Combining these methods with the structures and sizes of our robot, the ePSA lengths $\{l_1, l_2, l_3\}$ can be easily calculated from the parameters $\{k, \theta, \phi\}$ as

$$l_1 = 2\sin(\frac{l_c k}{2})(\frac{1}{k} - d\sin\phi), \tag{13}$$

$$l_2 = 2\sin(\frac{l_c k}{2})(\frac{1}{k} + d\sin(60^\circ + \phi)), \tag{14}$$

$$l_3 = 2\sin(\frac{l_c k}{2})(\frac{1}{k} - d\sin(30^\circ + \phi)). \tag{15}$$

IV. TRAJECTORY PLANNING

We continue with our assumption that the robot always has one end fixed in each crawling cycle. As shown in Fig. 7, when the robot crawls in the pipe, the body shape of the robot can be abstracted into two scenarios. The first scenario is that the robot can retain the straight shape after each crawling cycle in the constrained environment of the pipe, and the second scenario is that the robot can retain the curved shape achieved after the last inflation. The trajectory planning of the robot in the Cartesian space is divided into two steps:
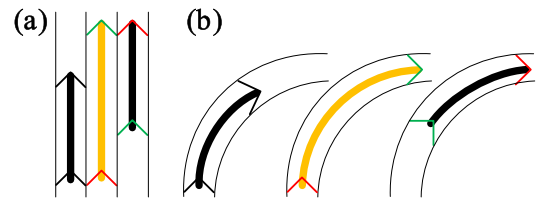

FIGURE 7. Two scenarios of the robotic body shape when crawling in the pipe. (a) straight shape, and (b) curve shape.

(1) Because the position of the rear foot is fixed during inflation, we can calculate the position of the frontal foot based on the target trajectory and the kinematics model in (10)-(15).

(2) Because the position of the frontal foot is fixed during deflation and the curvature of the deflated robot is the same as that after the last inflation, we can calculate the position of the rear foot by taking the initial ePSA length as the arc.

$$k_2 = k_1, \tag{16}$$

$$\theta_2 = (l_1 - 100)k_2, \tag{17}$$

$$\phi_2 = \phi_1, \tag{18}$$

where k_1, θ_1, and ϕ_1, are the configuration parameters; l_1 is the ePSA length of the robot after the last inflation; k_2, θ_2, and ϕ_2 are the configuration parameters of the robot after deflation.

In the backward locomotion, the frontal foot and rear foot are interchanged, and other calculation methods remain unchanged. The actual situation may be very complicated. After deflation, the curvature may not remain exactly the same as after inflation, but this method can be used as an ideal trajectory planning to provide a reference for actual real-time planning.
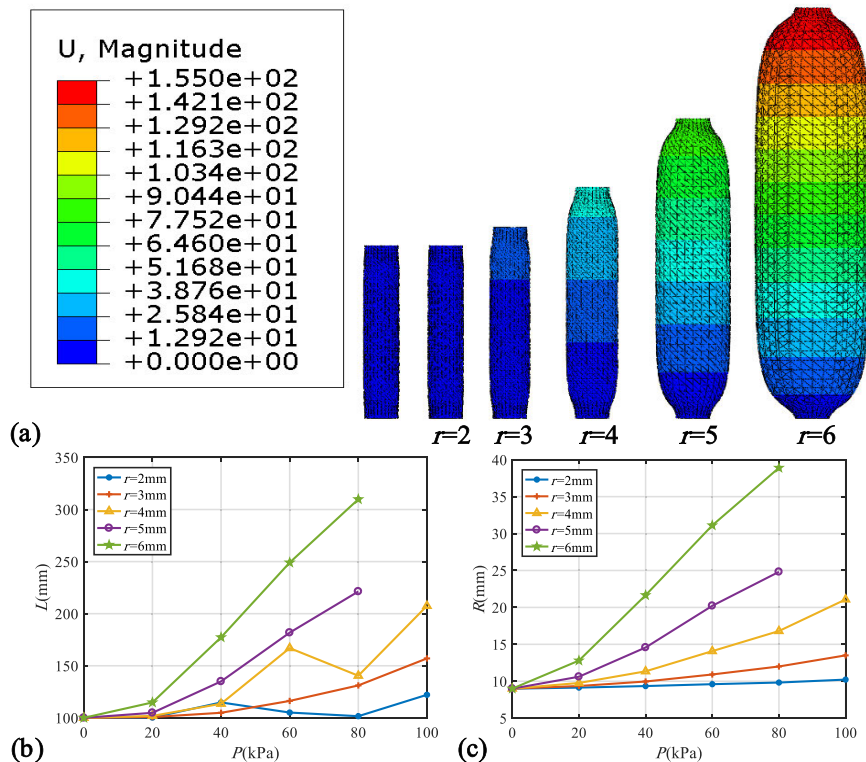
FIGURE 8. Finite element simulation of ePSA. (a) The ePSAs have different air chamber radii, r = 2mm, 3mm, 4mm, 5mm, 6mm, respectively; (b) the change of ePSA length L, and (c) the change of ePSA radius R without fiber wires, when the input air pressure changes from 0 to 100kPa, the step is 20kPa.

V. FINITE ELEMENT SIMULATIONS

A. SINGLE EXTENSIBLE PNEUMATIC SOFT ACTUATOR

A finite element method (FEM) model of the ePSA is developed to understand the nonlinear response of the ePSA and to select the optimal structural parameters.

The FEM model of the ePSA is developed by Abaqus/Standard. First, for creating the geometry modules, define the elastic body as a three-dimensional variability entity and the fiber wire as a three-dimensional variability line. Then, configure the material properties for the geometry modules. According to [40], the silicone rubber used by the robot can be defined as a hyperelastic material, and the fiber wire is defined as an elastic material. Next, the constraint relationship between the elastic body and the fiber wire is defined as the Tie connection. Finally, each ePSA module is meshed using solid tetrahedral quadratic hybrid elements (Abaqus element type C3D20H). Quadratic beam elements (Abaqus element type B32) are used for the thin fiber winding wire. Ignoring the effects of factors such as gravity and friction, pressure is applied to the entire air chamber in the Abaqus to simulate the inflated air pressure P with the atmospheric pressure P_a as the relative zero pressure point (P_a = 101.325 kPa). In the FEM model, the initial ePSA length is l_0 = 100 mm and the initial ePSA radius is R = 9 mm.

As shown in Fig. 8(b), the ePSA with an air chamber radius of r = 6 mm or r = 5 mm has better axial extension performance, but it cannot withstand a pressure of more than 80 kPa. The ePSA length with an air chamber radius of r = 4 mm or r = 2 mm fluctuates. This is because the extension and expansion alternately appear as the main deformation under different input pressure ranges. At the same time, Fig. 8(c) shows that the actuator with an air chamber radius of r = 3 mm has a relatively small radial expansion; therefore, r = 3 mm is selected as the optimum air chamber radius of the ePSA.

As shown in Fig. 9(b) and (c), winding of the fiber wires brings the relationship between the ePSA length and the input air pressure closer to a linear relationship. It is shown that the fiber winding wire effectively suppresses the radial expansion and enhances the axial extension performance of the ePSA. The reinforcing effect improves with increase in the number of winding turns. However, when the number is N = 50, N = 25, or N = 20, the reinforcing effect of ePSA length is not much different. Taking the fabrication process and the weight of the ePSA prototype into consideration, we choose N = 20 as the optimal number of fiber winding turns for the ePSA.

B. FLEXIBLE FOOT

The friction between the flexible feet of the robot and the pipe wall is a decisive condition that affects the robot motion and crawling speed in pipes.
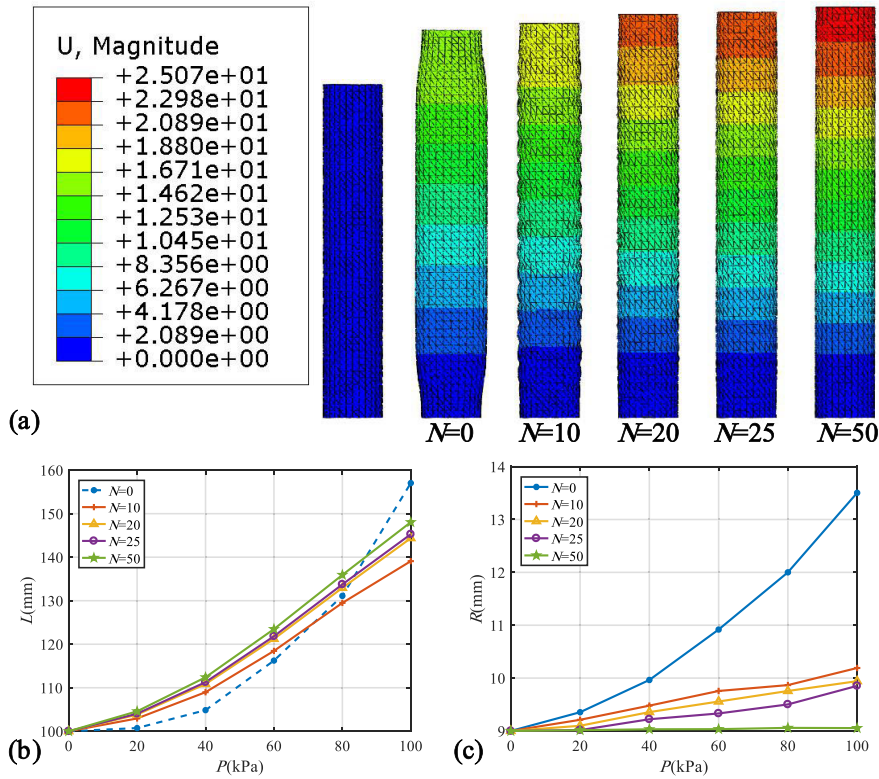
FIGURE 9. Finite element simulation of ePSA. (a) The ePSAs have different numbers of fiber winding turns, $N = 0$, 10, 20, 25, 50, respectively; (b) the change of ePSA length L, and (c) the change of ePSA radius R with fiber wires, when the input air pressure changes from 0 to 100kPa, the step is 20kPa.
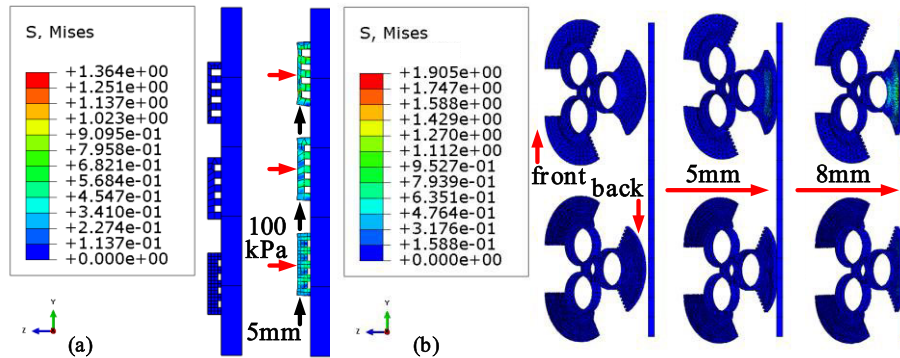
FIGURE 10. Finite element simulation of flexible foot. (a) The pressure of the groove segment is 100kPa and the displacement is 5mm; (b) the displacement of the foot is 5mm and 8mm, respectively.

The main factors that will affect the friction are the material hardness, the angle (as shown in Fig. 3), and the groove size of the foot. The finite element simulation of the foot is shown in Fig. 10. First, the effects of different groove heights on the stress and sliding friction of the groove surface are tested. Then, the stress and strain of the front smooth surface and back groove surface of the complete foot are tested.

The results show that under the same pressure, the sliding friction of the groove is almost independent of the groove height. However, as shown in Fig. 10(a), the stress and deformation increase with increase in the groove height. Considering the weight and service life of the flexible foot, we choose $h = 1$ mm as the optimal value of the groove height for the flexible foot. In actual applications, the contact between the foot and the pipe wall is very complicated and the pipe condition is different. And the friction coefficient is also different, which is difficult to simulate with FEM. Therefore, the material hardness and contact angle of the foot will be selected by the prototype crawling speed experiment.

C. PIPE-CRAWLING SOFT ROBOT

The foot radius d (as shown in Fig. 3) and number of connecting rings are important factors that affect the locomotion performance of the robot. In our previous study [30], we tested the effect of different radii on the performance of a 2D soft
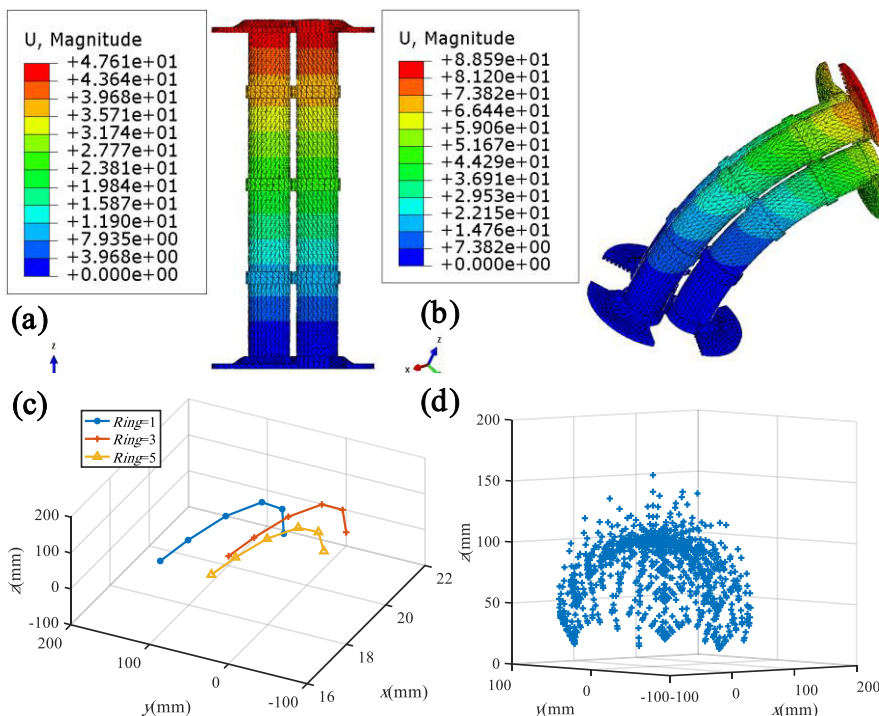
FIGURE 11. Finite element simulation of the robot. (a) Axial extension; (b) bending in 3D space; (c) tests of connecting ring ignoring the effects of gravity and friction. The input air pressure of ePSA1 changes from 0 to 100kPa, the step is 20kPa; the input air pressure of ePSA2 is 40kPa, and the input air pressure of ePSA3 is 60kPa; (d)simulation of crawling workspace.

robot. The results showed that the 2D robot can generate better bending performance when the radius is $d = 12$ mm or $d = 14$ mm. Considering the size of the endoscope camera, we select $d = 14$ mm in this paper. The coupling effect of the number of connecting rings on the bending of the robot is shown in Fig. 11. In the FEM model, the constraint relationship between the connecting ring, flexible foot, and ePSA is defined as the Tie connection. The results show that the robot has optimal extension and bending property when the number of connecting rings is 3. The workspace in Fig. 11(d) shows that, in theory, the robot has excellent active steering property and it can crawl through a 90º or smaller bending angle by switching the actuating pattern, i.e., the crawling gait of the soft robot.

In summary, the main structural parameters of the robot are determined through the three finite element simulations for realizing better locomotion performance along with consideration of ease of fabrication and weight of the prototype. The parameters are listed in Table 1.

VI. FABRICATION

A. SINGLE EXTENSIBLE PNEUMATIC SOFT ACTUATOR

The fabrication process of the ePSA can be divided into three steps, as shown in Fig. 12(a).

(1) Injection of elastic body: first, assemble the molds, including the cavity mold, side mold, and base mold, which are prepared by 3D printing. Second, inject the proportionally mixed silicone material (Ecoflex 00-50, Smooth-On). Finally,

TABLE 1. Optimal parameters of the pipe crawling soft robot.

Parameters	Value
ePSA length L_0/mm	100
ePSA radius R_0/mm	9
ePSA air chamber radius r_0/mm	3
Number of winding turns N	20
Foot groove height h/mm	1
Foot radius d/mm	14
Number of connecting rings	3

cover the upper surface with a steel plate to make the body wall thickness uniform and wait for it to become solidified at room temperature.

(2) Winding of fiber wires: after the silicone rubber is solidified, disassemble the molds and wind the fiber wires (Kevlar, DuPont) sequentially as a double helix trace on the elastic body. Then, apply a layer of silicone rubber gel evenly on the surface. The prototype is ready when the outer surface is also solidified.

(3) Apply the seal head (ABS, acrylonitrile butadiene styrene) to prevent air leakage by using the silicone adhesive glue (HJ-420). The fabricated ePSA is depicted in Fig. 12(b).
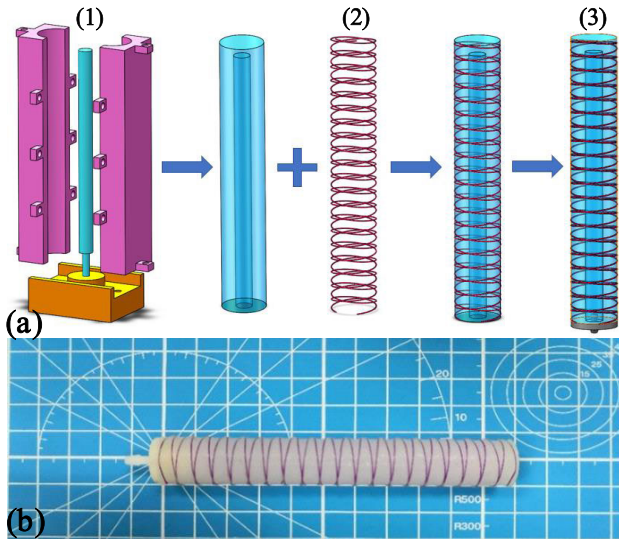
FIGURE 12. Fabrication process of the ePSA. (a) The ePSA is made in three steps, injecting the elastic body, winding the fiber wires, and applying the seal head; (b) a fabricated prototype of the ePSA.

B. PIPE-CRAWLING SOFT ROBOT

The final assembly of the robot is graphically shown in Fig. 13. Three ePSAs, three connecting rings (ABS), and two flexible feet are integrated into a single functional body. The maximum diameter of the robotic prototype is 78 mm and the minimum diameter is 46 mm. These dimensions are chosen empirically to create a prototype that is easily testable under laboratory conditions using off-the-shelf transparent pipes with diameters ranging from 55 mm to 75 mm. In addition, the foot is 3D printed with different rubber materials of different hardness. The prototype crawling speed experiment is performed to select the optimal material hardness and contact angle of the foot.
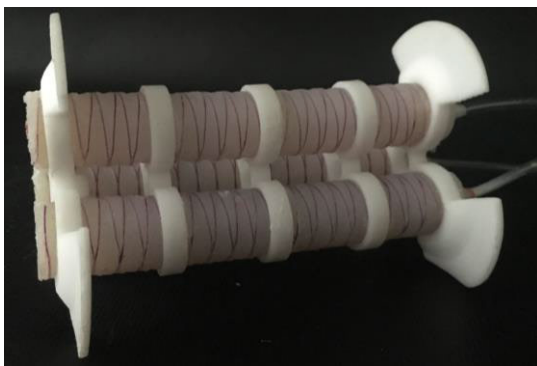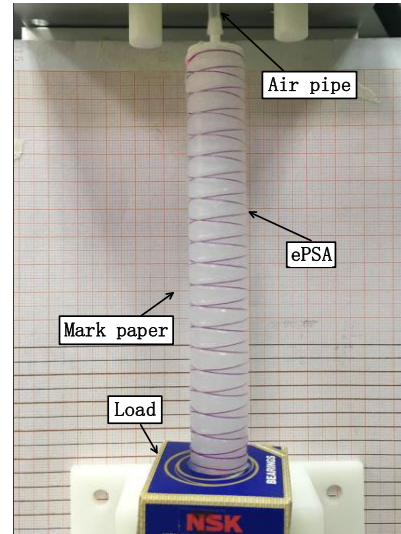

FIGURE 13. Prototype of the pipe crawling soft robot.

VII. EXPERIMENTS AND RESULTS

A. STATIC IDENTIFICATION OF ePSA

As shown in Fig. 14, the static identification experimental system is mainly composed of scale mark paper, ePSA, and load. The static identification experiment steps are as follows:

(1) Measure the initial ePSA length in the vertical direction.

FIGURE 14. Static identification experimental system of the ePSA.

(2) Measure the ePSA length while incrementing the pressure by 10 kPa from 10 kPa to 100 kPa. According to the finite element simulation of the robot and the practical application scenario, the air pressure range of 0–100 kPa and the atmospheric pressure as the relative zero pressure point could basically represent the normal working range of the robot.

(3) Change the load and repeat steps (1) and (2).

(4) Change the load again and repeat steps (1) and (2).

(5) Process the experimental data and fit the parameters k_p and f_p.

(6) Verify the accuracy of the statics model. If the static model is inaccurate, repeat the static identification experiment until the statics model is accurate.

First, the above static identification experiment is repeated three times and the identification data are averaged to ensure accuracy. Then, while maintaining constant air pressure, the parameters k_p and f_p are obtained by least square fitting with the load as the independent variable and the collected extension length data as the dependent variable. Furthermore, the parameters k_p and f_p at different pressures ranging from 10 kPa to 100 kPa are sequentially calculated. Finally, the relationships between the parameters k_p and f_p and the input air pressure P are identified by least square fitting again. The identification results of the three ePSAs are shown in Figs. 15 and 16.

The reason for segmenting the elastic parameter fitting curve is that the elastic force of the robot for generating axial extension mainly originates from the silicone material and the fiber winding wires. However, as the robot extends, the winding angle changes, which is not enough to maintain high elasticity. This means as the air pressure increases, the elastic force provided by the fiber winding wires become weakened. The silicone material is the main influencing factor for the elasticity. Nevertheless, it cannot provide the same elastic force as under smaller input air pressure.

The reason for segmenting the thrust parameter fitting curve is that the thrust increases with increase in the air
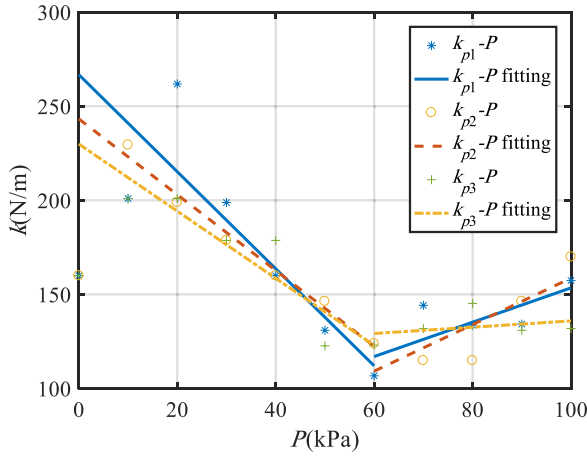
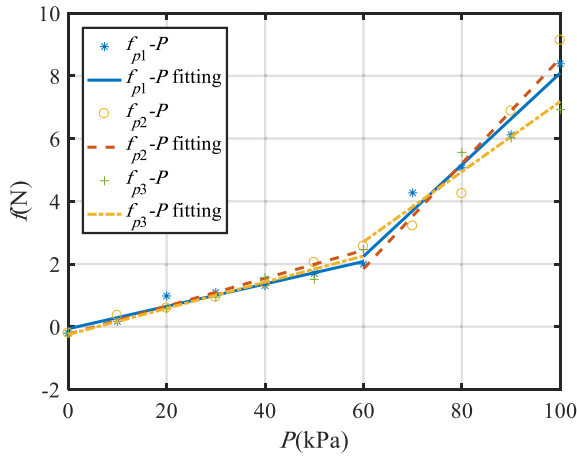**FIGURE 15. Identification result of elastic parameter K_{p}.**

FIGURE 16. Identification result of thrust parameter f_{p}.

pressure. Then, as the elastic action decreases, the binding force of the ePSA to return to the initial state becomes smaller. Therefore, after the critical point of 60 kPa, it can be considered that the robot is more likely to perform extension under increasing input air pressure.

By sequentially performing static identification experiments on the three ePSAs, the parameters in the statics model can be obtained as follows:

$$
k_{p1} = \begin{cases} -2.579 * P + 266.8 & P \le 60\text{kPa}, \\ 0.9125 * P + 62.19 & P > 60\text{kPa}, \end{cases} \tag{19}
$$

$$
f_{p1} = \begin{cases} 0.03575 * P - 0.06627 & P \le 60\text{kPa}, \\ 0.1463 * P - 6.534 & P > 60\text{kPa}, \end{cases} \tag{20}
$$

$$
k_{p2} = \begin{cases} -2.013 * P + 243.2 & P \le 60\text{kPa}, \\ 1.236 * P + 34.99 & P > 60\text{kPa}, \end{cases} \tag{21}
$$

$$
f_{p2} = \begin{cases} 0.0446 * P - 0.239 & P \le 60\text{kPa}, \\ 0.168 * P - 8.235 & P > 60\text{kPa}, \end{cases} \tag{22}
$$

$$
k_{p3} = \begin{cases} -1.784 * P + 229.9 & P \le 60\text{kPa}, \\ 0.167 * P + 119.2 & P > 60\text{kPa}, \end{cases} \tag{23}
$$

$$
f_{p3} = \begin{cases} 0.04175 * P - 0.2493 & P \le 60\text{kPa}, \\ 0.1118 * P - 4.002 & P > 60\text{kPa}. \end{cases} \tag{24}
$$

The statics models of the three ePSAs are compared with the prototype data and the finite element simulation results to verify their accuracy. As shown in Fig. 17, the main reason for the error between the prototype data and the finite element simulation result is the error between the actual and classical parameters of the material used by the ePSA. In addition, gravity affects the performance of the prototype.
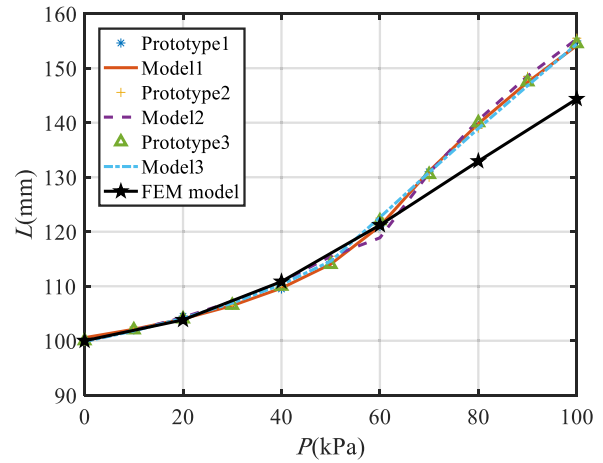

FIGURE 17. Comparison of ePSA length among statics model, simulation data, and prototype data.

On the other hand, the statics model of each ePSA is almost in agreement with the measured data of the prototype. The average error of the three ePSAs is only 0.51 mm. The distribution of specific error values is shown in Fig. 18; the maximum absolute error is only 3.62 mm. In most cases, the absolute error is only approximately ±1 mm. The results show that the established statics model is correct. The extension behaviors of the three ePSAs are similar, which indicates that the fabrication process is feasible. It is possible to quickly fabricate a plurality of ePSAs in a short time.
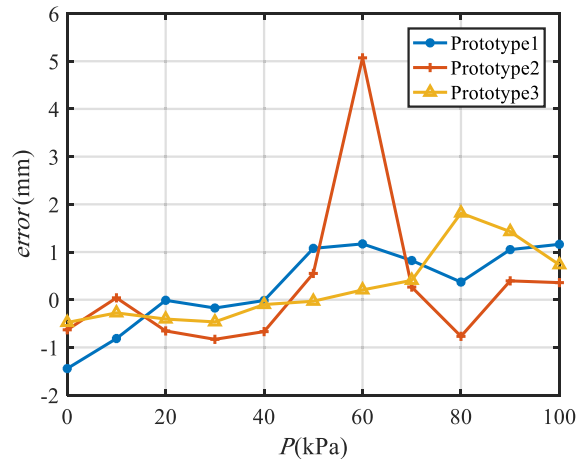

FIGURE 18. Error between statics model and prototype data of ePSA length.

Then, the output force of the ePSA is tested using a tiny S-type pressure sensor (500 g, ZNLBS) when the ePSA is maintained in its initial shape. As shown in Fig. 19, the output force of the ePSA increases as the input air pressure increases. The maximum output force is 8.42 N. The average error between the statics model and prototype data is only 0.28 N. It is further demonstrated that the method of static identification is feasible and the established statics model can describe the performance of the actuator accurately.
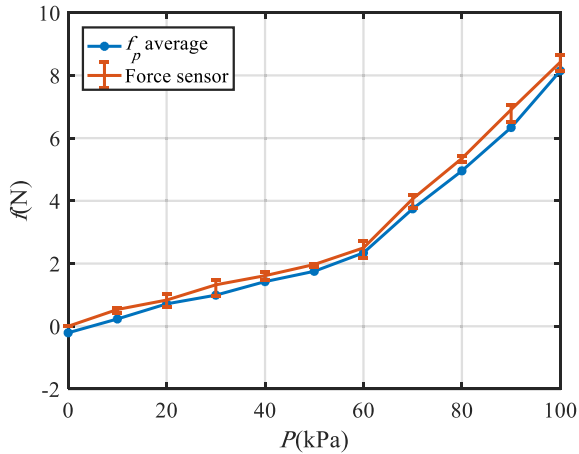
FIGURE 19. Comparison of output force between statics model and prototype data of the three ePSAs.

When the robot crawls through the pipe, the friction should be added into the statics model as

$$k_P y + m y + f_\mu = f_P, \quad (25)$$

where f_μ is the friction between the robot and the pipe wall. Comparing (25) to (3), the friction f_μ can be calculated by the difference in the extension length under the same input air pressure.

$$f_\mu = k_p(y_1 - y_2), \quad (26)$$

where y_1 and y_2 are the extension length outside and inside pipes, respectively.

B. EXPERIMENTAL SYSTEM FOR CRAWLING

The experimental system is mainly composed of a host PC, fluidic control board, DC power source, and the soft robot. The host PC is the main controller of the entire system. It provides gait switching signal for the fluidic control board. The fluidic control board is modified from the open source control system in the Soft Robotics Toolkit [47]. The main function of the board is to use the PWM (Pulse Width Modulation) modules, solenoid valves, air pumps, and air pressure sensors to realize the inflation and deflation of the robot, thereby controlling the crawling speed. The DC power is used to provide suitable working voltage for the fluid control board.

C. FOOT SELECTION

Because the material hardness and contact angle of the flexible foot directly affect the crawling efficiency of the robot,
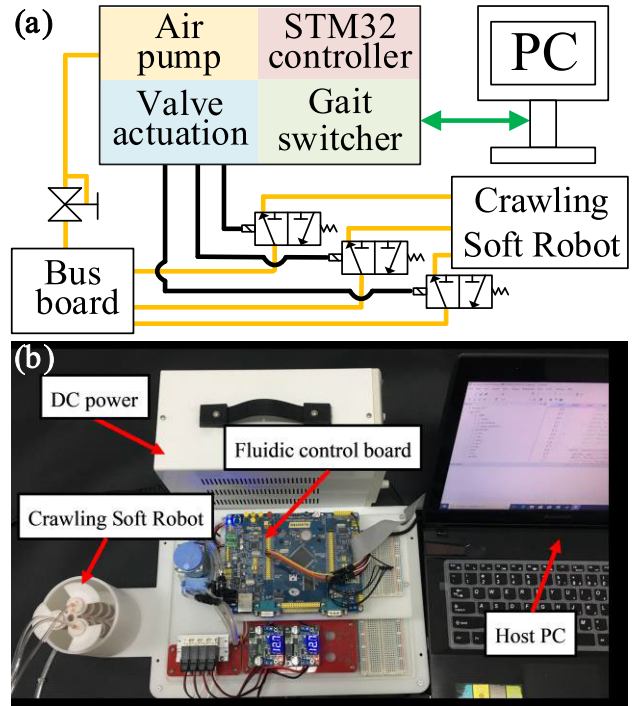
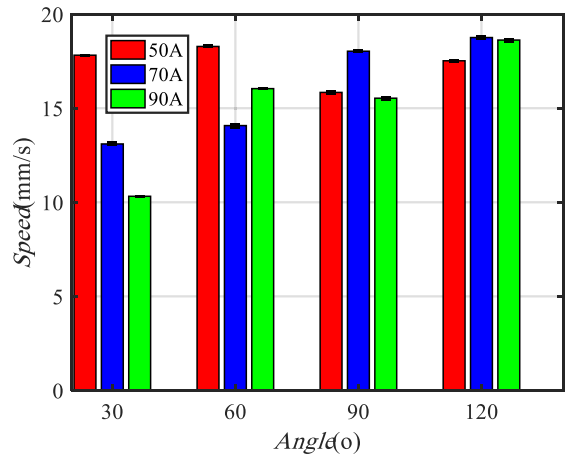**FIGURE 20.** Block diagram and physical connections of experimental system for crawling.

FIGURE 21. Crawling speed of robot with different flexible feet.

the feet are tested for horizontal crawling speed according to different material hardness and foot angles. The diameter of the pipe is 70 mm and each crawling cycle is 2 s. The experimental results are shown in Fig. 21. A desired crawling speed, that is, greater than 10 mm/s, can be obtained using material hardness between 50A and 70A (shore) and foot angle between 30° and 120°. With 70A hardness, the crawling speed of the robot increases with the increase in the foot angle. However, the creeping speed of the robot with other hardness values appears to fluctuate with increase in the foot angle. We choose the foot with Shore hardness of 70A and foot angle of 120° as the optimal foot for the robot. All subsequent experiments are performed with this type of foot.
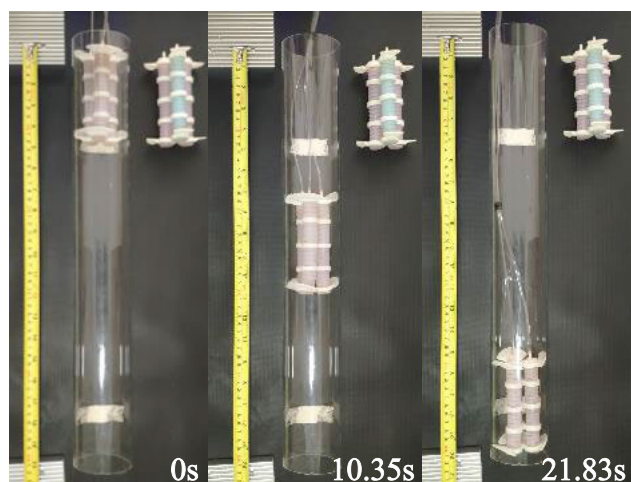
D. BASIC CRAWLING EXPERIMENTS

We perform the horizontal crawling experiment and vertical crawling experiment to test the forward and backward loco-motion ability of the robot. An L-shaped crawling experiment is also performed to test the active steering property and the trajectory planning method. In each experiment, the pipe diameter is 70 mm, the material of the pipe is acrylic, and each crawling cycle is 2 s to ignore the dynamic process of the robot.

1) HORIZONTAL CRAWLING

The result of the horizontal crawling experiment is shown in the photograph sequence in Fig. 22. The robot has forward crawling speed of 18.3 mm/s and backward crawling speed of 17.7 mm/s in a fixed gait. The forward crawling sliding friction is approximately 15.3 N and the backward crawl-ing sliding friction is approximately 16.9 N. The crawling speeds of the robot in pipes of other diameters are shown in Table 2. The crawling speed of the robot fluctuates because the friction between the foot and the pipe wall increases as the diameter of the pipe decreases. Moreover, the resistance, which prevents the robot from moving forward, becomes larger. On the contrary, the friction between the foot and the pipe wall decreases as the diameter of the pipe increases. The anchoring force of the robot becomes smaller and the forward locomotion becomes difficult. The optimal crawling diameter of the robot is 60 mm–70 mm. And because the contact surface of the robot is groove surface during backward loco-motion. The contact surface of the robot is smooth surface during forward locomotion. And the sliding friction of the groove surface is higher than the sliding friction of the smooth surface. Thus, the backward locomotion tends to slower than the forward locomotion. As shown in Table 2, the crawling speed of the soft robot is higher than that reported for several other types of crawling robots. In fact, this study sets a new record for the speed of peristaltic crawling robots according to our knowledge.

TABLE 2. Comparison of horizontal crawling speed.

Robot	Diameter(mm)	Crawling velocity(mm/s)	
Connolly *et al.* [19]	13	\	
Calderon *et al.* [20]	≈40	≈1.19	
Yamazaki *et al.* [21]	28	4.38	
Gilbertson *et al.* [22]	19	≈13.5	
Takeshima *et al.* [23]	2.6-6	6.7	
	Diameter	**Forward**	**Backward**
	55	17.4	15.9
	60	20.1	18.2
This paper	65	19.5	17.7
	70	18.3	16.7
	75	17.6	16.2

2) VERTICAL CRAWLING

The result of the vertical crawling experiment is shown in the photograph sequence in Fig. 23. The upward crawling speed is 12.9 mm/s and the downward crawling speed is 19.1 mm/s in a fixed gait. The robot can dynamically lift its own weight, 70.2 g. The maximum theoretical load of the robot is 2.456 kg according to the maximum output force of the ePSA, shown in Fig. 19.

$$M_{load} = (3 * F_{ePSA} - M_r g)/g, \qquad (27)$$

where M_{load} is theoretical load, F_{ePSA} is the output force of the ePSA, and M_r is the robot.
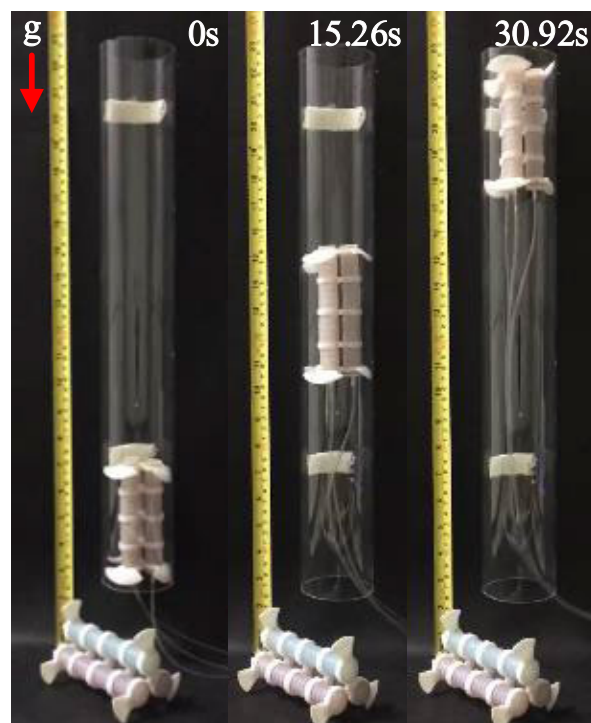
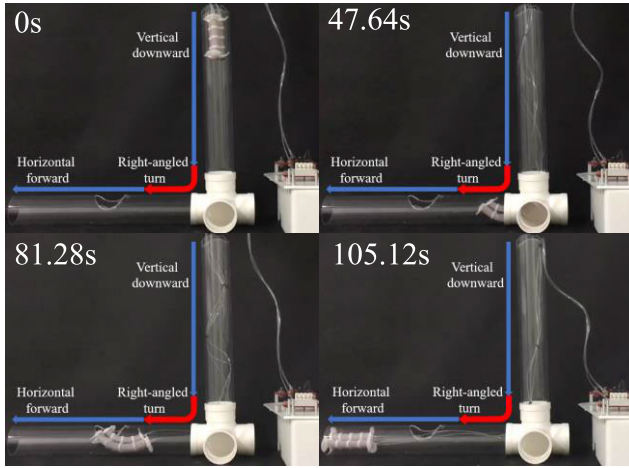**FIGURE 23.** Photograph sequence of vertical crawling.

FIGURE 22. Photograph sequence of horizontal crawling.

FIGURE 24. Photograph sequence of L-shaped crawling.

3) L-SHAPED CRAWLING

The result of the L-shaped crawling experiment is shown in the photograph sequence in Fig. 24. First, the robot crawls down the vertical pipe. Next, by switching the crawling gait, the robot changes its body shape to crawl through the right-angled elbow. Then, the robot continues to crawl forward through the horizontal pipe. Finally, by switching the gait again, the robot successfully exits the pipe through a gap.

The trajectory of the L-shaped crawling can be planned according to the trajectory planning method in Section IV. In Fig. 25(a), random trajectory refers to a trajectory randomly selected by the computer under the constraint of the pipe structure. There are tens of thousands of such trajectories. The ideal trajectory is the route with the least crawling cycle and the fastest crawling speed. Based on the ideal trajectory, the actuation sequence of the robot can be calculated by the inverse kinematics model. Then, the actual trajectory can be obtained by executing the actuation sequence offline.

In Fig. 25(b), the number of actuations when the robot crawls through the right-angled elbow is significantly higher than in the ideal trajectory. This is because the diameter of the elbow is larger and its surface is smoother because of which the friction between the foot and the elbow wall becomes smaller. With the ideal number of actuations and gait2, the robot cannot completely crawl through the elbow. The crawling gait is again switched to navigate the gap in the horizontal pipe. If gait1 is maintained, the frontal foot will be stuck in the gap. However, gait3 can help the robot to crawl through the gap. This shows that the robot has strong adaptability to crawling. In addition, the gaits are switched by supervision.

E. ADDITIONAL CRAWLING EXPERIMENTS
1) CRAWLING IN BELLOWS

In order to test the compliance of the robot, the crawling experiment in a bellows with diameter of 75 mm is performed, as shown in the photograph sequence of Fig. 26. If the body of the robot cannot be changed, the robot will be
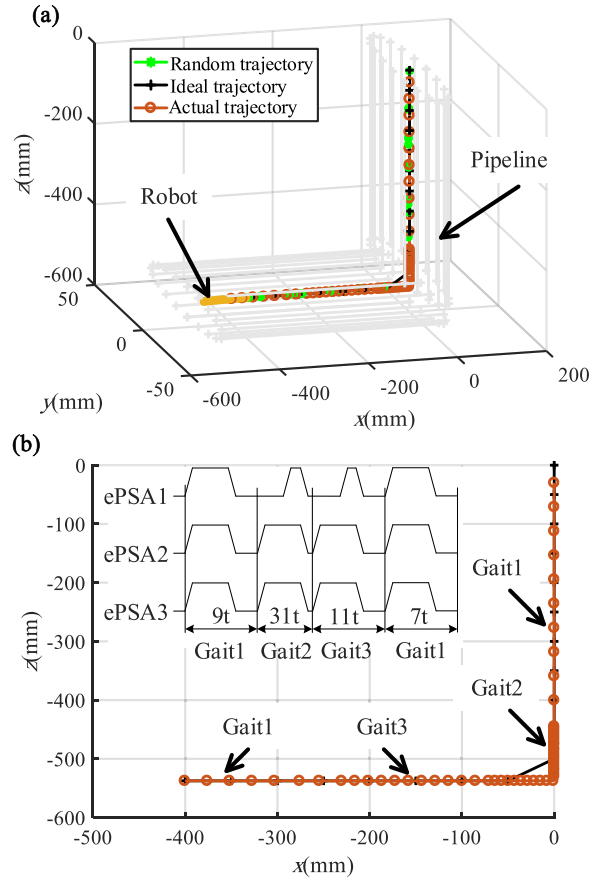

FIGURE 25. Trajectory planning of L-shaped crawling. This trajectory requires four gaits, Gait1 (the three ePSAs are simultaneously inflated for 1.5 s and deflated for 2 s), gait2 (ePSA2 and ePSA3 are inflated for 1.5 s, ePSA1 is inflated for 0.3 s, and then the three ePSAs are deflated but not fully for 0.2 s at the same time), and gait3 (ePSA2 and ePSA3 are inflated for 1.5 s, ePSA1 is inflated for 0.3 s, and then the three ePSAs are fully deflated for 0.5 s).
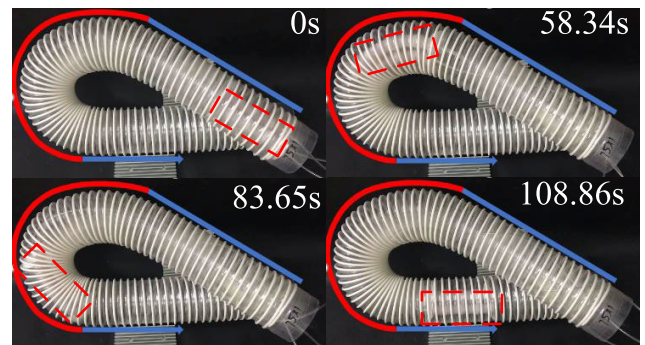
FIGURE 26. Photograph sequence of crawling in bellows.

stuck at the turn. However, the robot can crawl through the turn smoothly by switching the crawling gait. The minimum turning radius is 38.2 mm.

2) CRAWLING IN OPAQUE PVC PIPE

In order to test the inspection ability of the robot, the crawling experiment is performed in an opaque PVC (polyvinyl chloride) pipe with diameter of 75 mm, as shown in Fig. 27. The robot can relay the situation in the pipe in real time by

FIGURE 27. Photograph sequence of crawling in opaque PVC pipe.

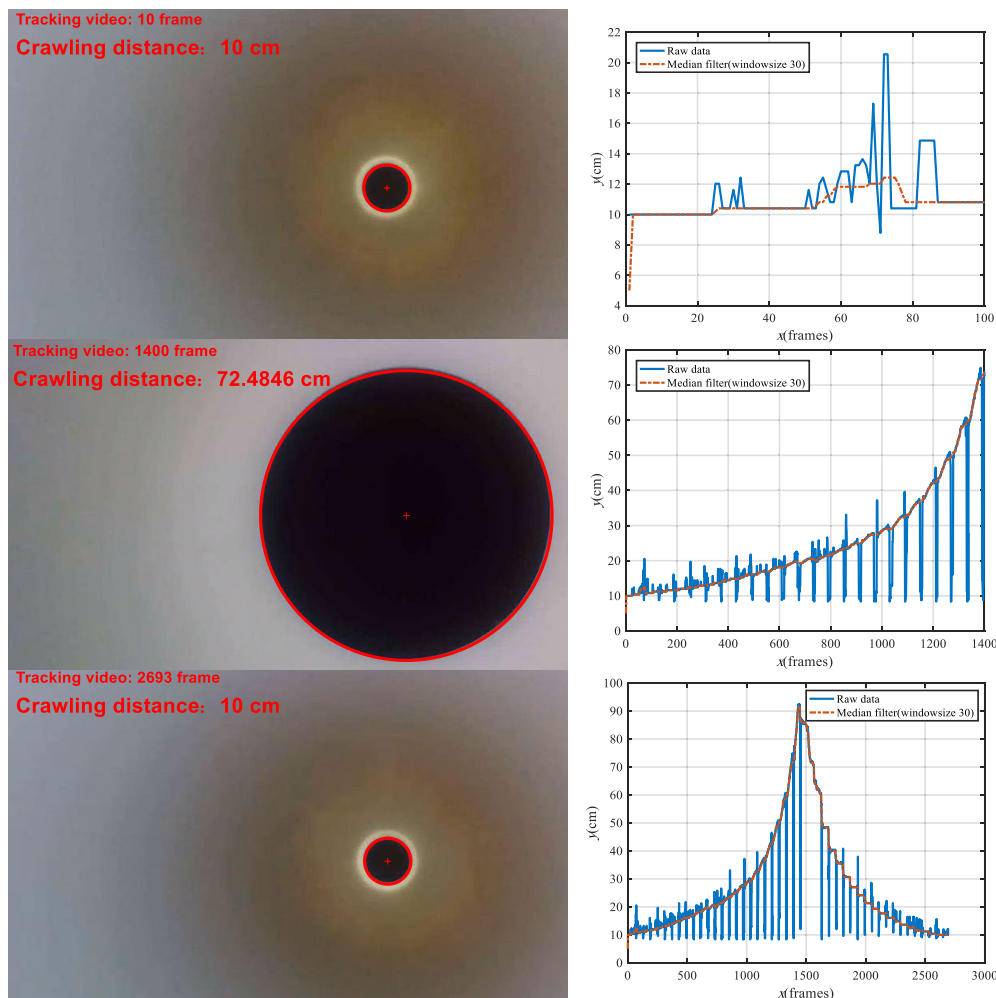means of an endoscopic camera carried by it. We can calculate the relative position of the robot in the pipe by detecting the radius of the pipe end in each frame of the video stream. The crawling distance fluctuates in the graph because of the jitter and blurriness during the inflation process, which results in inaccurate detection. The curve obtained after the median filtering process can better reflect the crawling distance of the robot.

3) CRAWLING ON TEXTURED SURFACE

In order to test the adaptability of the robot, the crawling experiment is performed on a textured surface, as shown in the photograph sequence in Fig. 28. The robot can crawl forward at a speed of 12.8 mm/s without the pipe.

The complete series of the basic and additional crawling experiments can be found in the supporting movie S1.mp4. Analysis of the movie shows that although the robot has high crawling speeds in the horizontal pipe and vertical pipe, it still consumes considerable time to turn. This phenomenon indicates that trajectory planning based on offline open-loop control has limitations, and efficient gait switching method
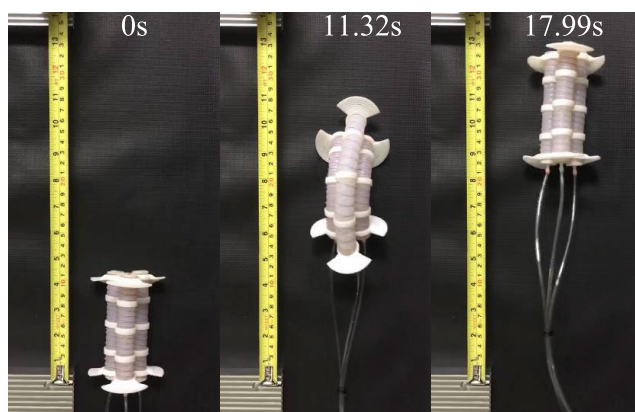

FIGURE 28. Photograph sequence of crawling on textured surface.

and feedback control are necessary, which is a matter of further research.

VIII. CONCLUSION

This study aimed to improve the pipe inspection performance of pipe-crawling soft robots. We presented a novel

pipe-crawling soft robot consisting of three extensible pneumatic soft actuators (ePSA), three connecting rings, a frontal foot, and a rear foot. We performed the structural design, finite element simulation, kinematics modeling, trajectory planning, prototype fabrication, and prototype experiments of the soft robot. As shown in Fig. 11(d), the simulation results of the crawling workspace of the soft robot provide convincing evidence of the three-dimensional motion of the robot. In theory, the robot has good steering property, and it can crawl through 90° or smaller bending angle by switching the gait, which depends on the input air pressure of the three ePSAs.

With regard to the problems in establishing a complete mathematical model of soft robots with a parallel structure, although some studies have employed 3D soft elastomers, few researchers have applied them to mobile robots. Moreover, the relationship between the input pressure and length of the actuator is often ignored by researchers. In this paper, the phenomenological modeling method is used to establish the statics model of the ePSA. Based on reverse thinking, the ePSA is equivalent to a three-element model consisting of a thrust element, a spring element, and a damping element in parallel. Then, based on the constant curvature method, the kinematics and inverse kinematics models of the robot are established. Finally, a highly precise mathematical model with limited computation and easy engineering application of the pipe-crawling soft robot is obtained.

According to the results of the crawling experiments in various scenarios, the proposed robot can crawl fast (>15 mm/s, which is higher than the speed of similar robots, as shown in Table 2), lift its own weight(70.2 g), has excellent steering property, adapts to complex pipelines, and perfectly completes the pipeline inspection by carrying an endoscope camera.

The proposed soft robot allows for a longer structure in series to further improve the steering property in pipes. Moreover, the robot can also be modified and scaled for various applications. In the future, we will further improve the intelligence and crawling speed of the robot through internal flexible sensors and closed-loop feedback control.

REFERENCES

[1] L. Boaz, S. Kaijage, and R. Sinde, "An overview of pipeline leak detection and location systems," in *Proc. 2nd Pan Afr. Int. Conf. Sci. Comput. Telecommun. (PACT)*, Arusha, Tanzania, Jul. 2014, pp. 133–137.

[2] A. S. Z. Abidin, M. H. Zaini, M. F. A. M. Pauzi, M. M. Sadini, S. C. Chie, S. Mohammadan, A. Jamali, R. Muslimen, M. F. Ashari, M. S. Jamaludin, and C. Y. Ming, "Development of cleaning device for in-pipe robot application," *Procedia Comput. Sci.*, vol. 76, pp. 506–511, Dec. 2015.

[3] P. Singh and G. K. Ananthasuresh, "A compact and compliant external pipe-crawling robot," *IEEE Trans. Robot.*, vol. 29, no. 1, pp. 251–260, Feb. 2013.

[4] L. Shao, Y. Wang, B. Guo, and X. Chen, "A review over state of the art of in-pipe robot," in *Proc. IEEE Int. Conf. Mechatronics Autom. (ICMA)*, Beijing, China, Aug. 2015, pp. 2180–2185.

[5] M. Kaneko, K. Hiyamizu, T. Tsuji, and N. Imamura, "Dynamic behavior of pipe inspection robot driven by fluid force," *Trans. Jap. Soc. Mech. Eng.*, vol. 63, no. 611, pp. 2368–2376, Jul. 1997.

[6] F. B. I. Alnaimi, A. A. Mazraeh, K. S. M. Sahari, K. Weria, and Y. Moslem, "Design of a multi-diameter in-line cleaning and fault detection pipe pigging device," in *Proc. IEEE Int. Symp. Robot. Intell. Sensors (IRIS)*, Langkawi, Malaysia, Oct. 2015, pp. 258–265.

[7] Y. Kim, D. Shin, J. Moon, and J. An, "Design and implementation of an optimal in-pipe navigation mechanism for a steel pipe cleaning robot," in *Proc. 8th Int. Conf. Ubiquitous Robot. Ambient Intell. (URAI)*, Incheon, South Korea, Nov. 2011, pp. 772–773.

[8] T. Oya and T. Okada, "Development of a steerable, wheel-type, in-pipe robot and its path planning," *Adv. Robot.*, vol. 19, no. 6, pp. 635–650, Apr. 2012.

[9] A. Kakogawa and S. Ma, "Stiffness design of springs for a screw drive in-pipe robot to pass through curved pipes and vertical straight pipes," *Adv. Robot.*, vol. 26, nos. 3–4, pp. 253–276, Apr. 2012.

[10] K. Isaki, A. Niitsuma, M. Konyo, F. Takemura, and S. Tadokoro, "Development of an active flexible cable by ciliary vibration drive for scope camera," in *Proc. IEEE/RSJ Int. Conf. Intell. Robots Syst. (IROS)*, Beijing, China, Oct. 2006, pp. 3946–3951.

[11] W. Neubauer, "A spider-like robot that climbs vertically in ducts or pipes," in *Proc. IEEE/RSJ Int. Conf. Intell. Robots Syst. (IROS)*, Munich, Germany, Sep. 1994, pp. 1178–1185.

[12] Q. Liu, Y. Li, T. Ren, and Y. Chen, "An active helical drive in-pipe robot," *Robot*, vol. 36, no. 6, pp. 711–718, Nov. 2014.

[13] S. Liu and W. Shang, "Design of the small screw locomotion in-pipe robot," *Machine*, vol. 36, no. 2, pp. 76–78, May 2009.

[14] J. Qiao, J. Shang, X. Chen, and Z. Luo, "Development of an inchworm in-pipe robot based on the cam self-locked principle," *J. Mech. Eng.*, vol. 46, no. 11, pp. 83–88, Jun. 2010.

[15] E. Rome, J. Hertzberg, F. Kirchner, U. Licht, and T. Christaller, "Towards autonomous sewer robots: The MAKRO project," *Urban Water*, vol. 1, no. 1, pp. 57–70, Mar. 1999.

[16] H. Ohno and S. Hirose, "Design of slim slime robot and its gait of locomotion," in *Proc. IEEE/RSJ Int. Conf. Intell. Robots Syst. (IROS)*, Maui, HI, USA, Nov. 2001, pp. 707–715.

[17] R. Bogue, "The role of robotics in non-destructive testing," *Ind. Robot*, vol. 37, no. 5, pp. 421–426, Aug. 2010.

[18] G. Bao, H. Fang, L. Chen, Y. Wan, F. Xu, Q. Yan, and L. Zhang, "Soft robotics: Academic insights and perspectives through bibliometric analysis," *Soft Robot.*, vol. 5, no. 3, pp. 229–241, Jun. 2018.

[19] F. Connolly, P. Polygerinos, C. J. Walsh, and K. Bertoldi, "Mechanical programming of soft actuators by varying fiber angle," *Soft Robot.*, vol. 2, no. 1, pp. 26–32, Mar. 2015.

[20] A. A. Calderón, J. C. Ugalde, J. C. Zagal, and N. O. Pérez-Arancibia, "Design, fabrication and control of a multi-material-multi-actuator soft robot inspired by burrowing worms," in *Proc. IEEE Int. Conf. Robot. Biomimetics (ROBIO)*, Qingdao, China, Dec. 2016, pp. 31–38.

[21] S. Yamazaki, Y. Tanise, Y. Yamada, and T. Nakamura, "Development of axial extension actuator for narrow pipe inspection endoscopic robot," in *Proc. IEEE/SICE Int. Symp. Syst. Integr. (SII)*, Sapporo, Japan, Dec. 2016, pp. 634–639.

[22] M. D. Gilbertson, G. McDonald, G. Korinek, J. D. Van de Ven, and T. M. Kowalewski, "Serially actuated locomotion for soft robots in tube-like environments," *IEEE Robot. Autom. Lett.*, vol. 2, no. 2, pp. 1140–1147, Apr. 2017.

[23] H. Takeshima and T. Takayama, "Six-braided tube in-pipe locomotive device," in *Proc. IEEE/RSJ Int. Conf. Intell. Robots Syst. (IROS)*, Hamburg, Germany, Oct. 2015, pp. 1125–1130.

[24] H. Takeshima and T. Takayama, "Geometric estimation of the deformation and the design method for developing helical bundled-tube locomotive devices," *IEEE/ASME Trans. Mechatronics*, vol. 23, no. 1, pp. 223–232, Feb. 2018.

[25] T. Takayama, H. Takeshima, T. Hori, and T. Omata, "A twisted bundled tube locomotive device proposed for in-pipe mobile robot," *IEEE/ASME Trans. Mechatronics*, vol. 20, no. 6, pp. 2915–2923, Dec. 2015.

[26] D. Trivedi, C. D. Rahn, W. M. Kier, and I. D. Walker, "Soft robotics: Biological inspiration, state of the art, and future research," *Appl. Bionics Biomech.*, vol. 5, no. 3, pp. 99–117, 2008.

[27] L. Hao, C. Xiang, M. E. Giannaccini, H. Cheng, Y. Zhang, S. Nefti-Meziani, and S. Davis, "Design and control of a novel variable stiffness soft arm," *Adv. Robot.*, vol. 32, no. 11, pp. 605–622, May 2018.

[28] A. Al-Ibadi, S. Nefti-Meziani, and S. Davis, "Design, implementation and modelling of the single and multiple extensor pneumatic muscle actuators," *Syst. Sci. Control Eng.*, vol. 6, no. 1, pp. 80–89, Mar. 2018.

[29] Z. Gong, Z. Xie, X. Yang, T. Wang, and L. Wen, "Design, fabrication and kinematic modeling of a 3D-motion soft robotic arm," in *Proc. IEEE Int. Conf. Robot. Biomimetics (ROBIO)*, Qingdao, China, Dec. 2016, pp. 509–514.

[30] X. Wang, T. Geng, Y. Elsayed, C. Saaj, and C. Lekakou, "A unified system identification approach for a class of pneumatically-driven soft actuators," *Robot. Autom. Syst.*, vol. 63, no. 1, pp. 136–149, Jan. 2015.

[31] D. Trivedi, A. Lotfi, and C. D. Rahn, "Geometrically exact models for soft robotic manipulators," *IEEE Trans. Robot.*, vol. 24, no. 4, pp. 773–780, Aug. 2008.

[32] T. Zheng, D. T. Branson, E. Guglielmino, and D. G. Caldwell, "A 3D dynamic model for continuum robots inspired by an octopus arm," in *Proc. IEEE Int. Conf. Robot. Autom. (ICRA)*, Shanghai, China, May 2011, pp. 3652–3657.

[33] E. Tatlicioglu, I. D. Walker, and D. M. Dawson, "Dynamic modelling for planar extensible continuum robot manipulators," in *Proc. IEEE Int. Conf. Robot. Autom. (ICRA)*, Roma, Italy, Apr. 2007, pp. 1357–1362.

[34] P. Qi, C. Qiu, H. Liu, J. S. Dai, L. D. Seneviratne, and K. Althoefer, "A novel continuum manipulator design using serially connected double-layer planar springs," *IEEE/ASME Trans. Mechatronics*, vol. 21, no. 3, pp. 1281–1292, Nov. 2016.

[35] C. Laschi, M. Cianchetti, B. Mazzolai, L. Margheri, M. Follador, and P. Dario, "Soft robot arm inspired by the octopus," *Adv. Robot.*, vol. 26, no. 7, pp. 709–727, 2012.

[36] D. B. Reynolds, D. W. Repperger, C. A. Phillips, and G. Bandry, "Modelling the dynamic characteristics of pneumatic muscle," *Ann. Biomed. Eng.*, vol. 31, no. 3, pp. 310–317, Mar. 2003.

[37] R. J. Webster, III, and B. A. Jones, "Design and kinematic modeling of constant curvature continuum robots: A review," *Int. J. Robot. Res.*, vol. 29, no. 13, pp. 1661–1681, Jun. 2010.

[38] B. A. Jones and I. D. Walker, "Kinematics for multisection continuum robots," *IEEE Trans. Robot.*, vol. 22, no. 1, pp. 43–55, Feb. 2006.

[39] Y. Elsayed, C. Lekakou, T. Geng, and C. M. Saaj, "Design optimisation of soft silicone pneumatic actuators using finite element analysis," in *Proc. IEEE/ASME Int. Conf. Adv. Intell. Mechatronics (AIM)*, Besacon, France, Jul. 2014, pp. 44–49.

[40] Z. Zhang, S. Wang, X. Wang, H. Liu, and B. Liang, "Kinematic analysis of novel soft robotic arm based on virtual work principle," in *Proc. IEEE Int. Conf. Robot. Biomimetics (ROBIO)*, Kuala Lumpur, Malaysia, Dec. 2018, pp. 984–990.

[41] D. F. Moore, *The Friction and Lubrication of Elastomers*. Oxford, U.K.: Pergamon, 1972.

[42] K. A. Grosch, "The relation between the friction and viscoelastic properties of rubber," *Rubber Chem. Techn.*, vol. 37, no. 2, pp. 386–403, May 1964.

[43] T. Umedachi and B. A. Trimmer, "Design of a 3D-printed soft robot with posture and steering control," in *Proc. IEEE Int. Conf. Robot. Autom. (ICRA)*, Hong Kong, China, May 2014, pp. 2874–2879.

[44] J. Wu, J. Huang, Y. Wang, and K. Xing, "Nonlinear disturbance observer-based dynamic surface control for trajectory tracking of pneumatic muscle system," *IEEE Trans. Control Syst. Technol.*, vol. 22, no. 2, pp. 440–455, Mar. 2014.

[45] Z. Zhang, X. Wang, H. Liu, S. Wang, and B. Liang, "Nonlinear dynamic and effect parameters analysis for extension pneumatic muscle," in *Proc. 30th Chin. Control Decis. Conf. (CCDC)*, Shenyang, China, Jun. 2018, pp. 4437–4442.

[46] W. McMahan, B. Jones, I. Walker, V. Chitrakaran, A. Seshadri, and D. Dawson, "Robotic manipulators inspired by cephalopod limbs," in *Proc. Can. Design Eng. Netw. Conf.* Montreal, QC, Canada: McGill Univ., Jul. 2004, pp. 401–410.

[47] Harvard University, "Soft robotics 'toolkit' features everything a robot-maker needs," *Soft Robot.*, vol. 1, no. 3, pp. 224–230, Sep. 2014.

ZHIYUAN ZHANG received the B.S. degree in automation engineering from the Hefei University of Technology, Hefei, China, in 2017. He is currently pursuing the M.S. degree in control engineering with the Tsinghua Shenzhen International Graduate School, Shenzhen, China.

His research interests include design, modeling, and control of pneumatic soft robot.

XUEQIAN WANG received the B.S. degree from the Department of Mechanical Design Manufacturing and Automation, Harbin University of Science and Technology, Harbin, China, in 2003, the M.S. degree from the Department of Mechatronics and Automation, in 2006, and the Ph.D. degree in control science and engineering from the Harbin Institute of Technology Shenzhen Graduate School, Shenzhen, China, in 2010.

He is currently an Associate Professor with the Tsinghua Shenzhen International Graduate School, Shenzhen. His research interests include space robotics and teleoperation.

SONGTAO WANG received the B.S., M.S., and Ph.D. degrees in mechanical engineering from the China University of Mining and Technology, Xuzhou, China, in 2010, 2013, and 2017, respectively.

He is currently a Postdoctoral Researcher with the Research Institute of Tsinghua University at Shenzhen, Shenzhen, China. His research interests include intelligence robotics, continuum robotics, dynamic modeling, and control.

DESHAN MENG received the B.S. degree in mechatronics engineering from the Liaoning University of Science and Technology, Anshan, China, in 2011, and the M.S. and Ph.D. degrees in control science and engineering from the Shenzhen Graduate School, Harbin Institute of Technology, Shenzhen, China, in 2013 and 2017, respectively.

He is currently a Postdoctoral Researcher with the Tsinghua Shenzhen International Graduate School, Shenzhen. His research interests include space robotics, continuum robotics, dynamic modeling, and control.

BIN LIANG (M'97) received the B.S. and M.S. degrees in control engineering from Northwestern Polytechnical University, Xi'an, China, in 1991 and 1994, respectively, and the Ph.D. degree in precision instrument and mechanology from Tsinghua University, Beijing, China, in 1994.

He is currently a Professor with the Department of Automation, Tsinghua University. His research interests include space robotics, manipulators, and intelligent control.

• • •